ACS APPLIED MATERIALS & INTERFACES

RESEARCH ARTICLE

www.acsami.org

Photoluminescence of Dense Nanocrystalline Titanium Dioxide Thin Films: Effect of Doping and Thickness and Relation to Gas Sensing

Candy Mercado,[†] Zachary Seeley,[‡] Amit Bandyopadhyay,[‡] Susmita Bose,[‡] and Jeanne L. McHale*[,†]

[†]Chemistry Department and [‡]School of Mechanical and Materials Engineering, and Materials Science and Engineering Program, Washington State University, Pullman, Washington 99164, United States

Supporting Information

ABSTRACT: The photoluminescence (PL) of dense nanocrystalline (anatase) TiO_2 thin films is reported as a function of calcination temperature, thickness, and tungsten and nickel doping. The dependence of the optical absorption, Raman spectra, and PL spectra on heat treatment and dopants reveals the role of oxygen vacancies, crystallinity, and phase transformation in the performance of TiO_2 films used as gas sensors. The broad visible PL from defect states of compact and undoped TiO_2 films is found to be much brighter and less sensitive to the presence of oxygen than that of mesoporous films. The dense nanocrystalline grains and the nanoparticles comprising the mesoporous film are comparable in size, demonstrating the importance of film morphology and carrier transport in determining the intensity of defect photoluminescence. At higher calcination temperatures, the transformation to rutile results in the appearance of a dominant near-infrared peak. This characteristic change in the shape of the PL spectra demonstrates efficient capture of conduction band electrons by the emerging rutile phase. The W-doped samples show diminished PL with quenching on the red side of the emission spectrum occurring at lower concentration and eventual disappearance of the PL at higher W concentration. The results are discussed within the context of the performance of the TiO_2 thin films as CO gas sensors and the chemical nature of luminescent defects.

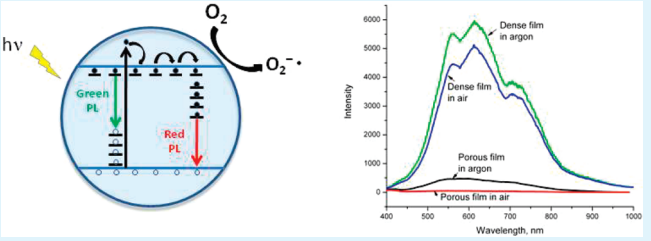

KEYWORDS: dense nanocrystalline film, titanium dioxide, photoluminescence, gas sensors, Ni-doping, W-doping

INTRODUCTION

Nanoparticulate TiO_2 has several physical properties that can make it an ideal gas sensing material such as good thermal stability, high surface area, and most importantly, electrical resistance that depends on the presence of oxidizing and reducing gases. For TiO_2, intrinsic oxygen vacancies are responsible for the n-type semiconducting properties.[1] In the common bulk phase of TiO_2, i.e., rutile, conductivity decreases with increasing partial pressure of O_2 and increases with the number of donor states associated with oxygen vacancy formation.[2,3] The removal of an oxygen atom leaves behind its associated −2 charge leading to defects such as Ti^{3+} centers and F^+ and F centers where one or two electrons, respectively, are trapped at vacancies.[4] Using Kroeger−Vink notation, oxygen vacancy formation can be represented as

$$2TiO_2 \rightarrow 2Ti_{Ti}^{x} + 3O_O^{x} + V_O^{\bullet\bullet} + \frac{1}{2}O_2 + 2e' \qquad (1)$$

O_2 adsorption at these surface oxygen vacancies then leads to the formation of O_2^-, O^-, or O^{2-} species,[5] resulting in electron scavenging and an increase in resistivity. Conversely, reducing gases such as CO, which react with adsorbed oxygen species, decrease the film resistivity.[6]

A variety of optical spectroscopic techniques have revealed the presence of different kinds of electron and hole traps associated with defects.[7,8] We have recently reported the visible defect PL of nanocrystalline TiO_2 that is observed on illumination with photon energies above the band gap of 3.2 eV.[9−11] By observing the PL of mesoporous TiO_2 films prepared from nanocrystalline anatase in the presence of electron and hole scavengers, we have resolved the overall broad visible PL into contributions from hole and electron traps.[10] The PL that peaks at a green wavelength, ∼530 nm, is assigned to the recombination of mobile (conduction band and shallow-trapped) electrons with trapped holes. The PL from the recombination of trapped electrons with valence band holes, on the other hand, extends into the red and near-infrared with a peak between 600 and 650 nm. Conditions that favor an increase in the number of mobile electrons, such as vacuum annealing to create n-donors in the form of oxygen vacancies, result in increased emission at green wavelengths.[11,12]

The PL of the rutile phase of TiO_2, on the other hand, occurs in the near-IR and is much brighter and narrower than the PL spectrum of anatase. Nakato et al. have assigned the rutile PL at ∼840 nm to recombination of conduction band electrons with holes trapped on oxygen atoms on the (110) and (100) facets.[13] In commercially available P25 nanoparticles (Aeroxide from Degussa), which contain about 75% anatase and 25% rutile, PL

Received: February 17, 2011
Accepted: June 24, 2011
Published: June 24, 2011

associated with red-emitting electron traps of anatase is apparently quenched, as is the rutile PL, and only the green emission from hole traps is observed.[9] Nanocrystalline anatase in the presence of hole scavengers such as ethanol gives rise to PL similar to that of P25 as the recombination of the trapped electrons is suppressed.[10] Conversely, thermally treated anatase films containing only minor amounts of rutile show a PL spectrum dominated by the minority phase, owing to facile interphasial electron transport and the much larger quantum yield for rutile PL as opposed to that of anatase. Thus, the intensity of PL depends not only on the concentration of luminescent traps but also on the ease with which nascent electron−hole pairs can be separated. The electron and hole traps of nano-TiO_2 strongly influence carrier transport in nanoparticulate TiO_2[14] as well as the binding of adsorbates that influence this carrier transport. Photoluminescence spectroscopy is therefore a useful technique for investigating the physical basis for the performance of TiO_2-based gas sensors that respond through changes in conductivity.

We have recently reported a study of nanocrystalline TiO_2 thin films as sensors of O_2 and CO.[15] In that work, it was found that increasing calcination temperature from 600 to 800 °C resulted in decreasing gas sensing performance and increased activation energy for electronic conduction, both of which were attributed to decreased surface area as revealed by XRD and SEM. Films calcined at 900 °C showed further decrease in performance and the emergence of the rutile phase. It was hypothesized on the basis of results of ref 15 that crystallinity of the TiO_2 film influences the adsorption and desorption of O_2, a key aspect of sensing performance. In the present work, we exploit the dependence of PL intensity on the density of defects and carrier transport to further examine the microscopic basis for gas sensing performance of films calcined at different temperatures. The ability of oxygen to scavenge conduction band electrons and decrease PL intensity provides a direct link to sensing performance. We also include a study of the PL from Ni- and W-doped films as it relates to their performance as sensors.[34] The PL results presented here shed light on the basis for superior performance of W-doped TiO_2 as a gas sensor. For the undoped films, we find striking differences between the PL of compact anatase films compared to that of previously studied mesoporous films, revealing the importance of transport in determining the intensity of trap state PL. Our results shed light on the physical basis for trap state luminescence, while revealing how dopants and thermal treatment influence sensor performance.

EXPERIMENTAL SECTION

Titanium-based metal−organic sols were created by dissolving titanium(IV) isopropoxide ($Ti[OCH(CH_3)_2]_4$ 97% min., Alfa Aesar) in 2-methoxyethanol ($CH_3OCH_2CH_2OH$ 99.3+%, Alfa Aesar) in an argon atmosphere. Tungsten(VI)isopropoxide ($W[OCH(CH_3)_2]_6$, Alfa Aesar) and nickel(II) methoxyethoxide ($Ni(OCH_2CH_2OCH_3)_2$, Alfa Aesar) were used as the dopant sources. Sols were created with metal ion compositions of 0, 2.5, 5, 10 at.% W and 10 at.% Ni balanced by Ti. Metal ionic concentration was kept at 0.5 M for all sols. The solutions were refluxed in an oil bath at 120 °C for 6 h under constant argon flow to ensure homogeneity.

TiO_2-based thin films were created by spin-coating the Ti sols onto a quartz substrate as described in more detail in ref 15. Films were created in two thicknesses by controlling the number of spin coated depositions: 2 or 12 layers. After every fourth deposition, the films were calcined, oxidized, and crystallized in a furnace between 600 and 900 °C. Cross-sectional SEM images showed no evidence of layers after calcination, as expected for this solution-phase deposition process.[34] Film resistance and gas sensing measurements were performed in a quartz tube furnace with controlled flowing gas atmosphere and temperature. Scanning electron microscope and X-ray diffraction techniques were used to characterize the morphology and crystal structure.

UV−visible absorption spectra of thin films were measured using a UV-2501PC Shimadzu spectrophotometer scanning from 800 to 250 nm. The Raman spectra were measured using 5 mW 413.1 nm Kr+ excitation, a double monochromator, and a PMT detector. The photoluminescence spectra were taken in backscattering geometry using a 20 mW 350.7 nm Kr+ excitation with a 385 nm long pass filter before the slit of an ACTON SpectraPro 2300i spectrometer.

RESULTS AND DISCUSSION

1. Characterization of Dense Nanocrystalline TiO_2 Films. The X-ray diffraction (XRD), Raman spectra, and field emission scanning electron microscopy (FE-SEM) images of undoped dense TiO_2 films calcined at 600, 700, 800, and 900 °C are shown in Figures S1, S2, and S3 the Supporting Information, respectively. The images confirm that the undoped films have little porosity compared to the ∼50% porosity of the nanocrystalline films, which were the subject of previous photoluminescence studies.[9−11] The presence of rutile in the anatase phase is an important aspect of gas sensing performance.[35] The XRD and Raman data of Figures S1 and S2 of the Supporting Information show that the samples calcined at 600, 700, and 800 °C are predominantly in the anatase phase, while the XRD of the 900 °C shows the emergence of rutile. However, as shown below, the PL spectrum of mixed-phase samples is much more sensitive to the presence of minor amounts of rutile than is XRD or Raman, and rutile PL will be evident in the film calcined at 800 °C.

The resistivity properties of undoped dense TiO_2 films calcined at 600, 700, 800, and 900 °C were previously reported, based on TiO_2 films prepared by a citrate−nitrate synthetic procedure.[15] The best sensing response was achieved with a film calcined at 800 °C and was attributed to crystallization of amorphous material to the anatase phase. For films prepared using the same procedure as used here, the best sensors were those based on films that had been calcined at 600−700 °C (Figure 5).[34] Film morphology is an important aspect of sensor performance.[36] The FE-SEM images shown in Figure S3 of the Supporting Information reveal little porosity and grain sizes that increase from about 60 to 150 nm for calcination at 600 to 900 °C, respectively. XRD measurements showed an increase in cystallinity between 600 and 700 °C, grain growth between 700 and 800 °C, and the onset of rutile formation in the 900 °C sample.

Previous work with thin film sensors[15] and the characterization data of Figures S1−S3 of the Supporting Information are for 12-layer films, while the optical absorption spectra reported below in Figure 4 are for 2-layer films. Each spin-coated layer contributes between 70 and 80 nm to the film thickness, and therefore, the 12-layer and 2-layer films are about 800−1000 nm and 140−160 nm thick, respectively. The 2-layer films were prepared in order to be able to determine the optical absorption in transmission.

2. Photoluminescence of Undoped Thin Films. Figure 1 compares the PL spectrum of a dense TiO_2 film calcined at 600 °C to that of a mesoporous TiO_2 film prepared from 6 nm anatase particles sintered at 450 °C according to the procedure of ref 16. Both samples are in the anatase phase, and the shapes of

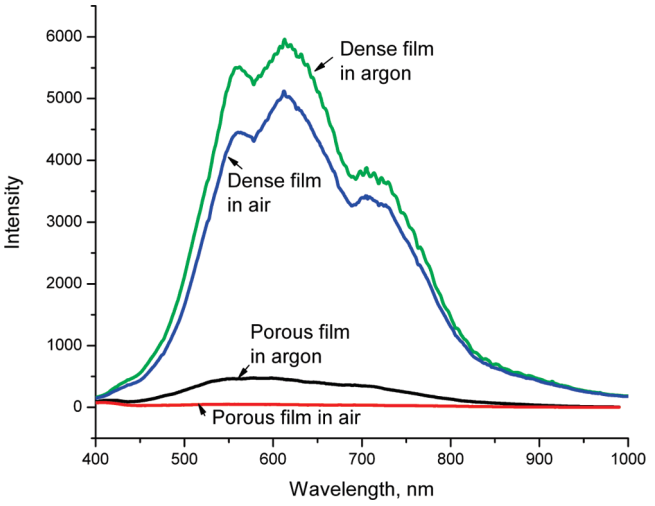

Figure 1. PL from a 12-layer dense nanocrystalline TiO_2 film, calcined at 600 °C, in air and in argon compared to that from a mesoporous anatase film in air and in argon.

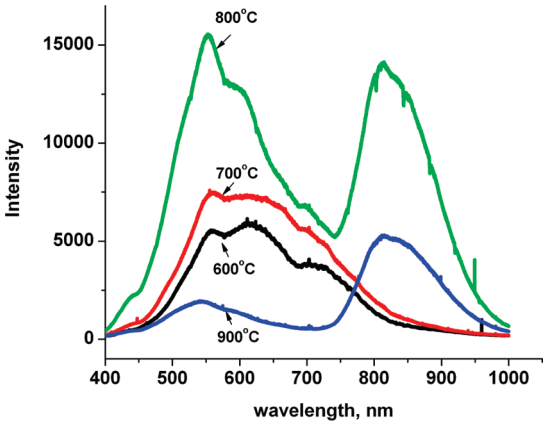

Figure 2. PL of dense 12-layer nanocrystalline TiO_2 films, excited at 350 nm and recorded in argon, as a function of calcination temperature.

their PL spectra are similar. The apparent structure in the emission spectrum of the thin film sample is a result of interference, as shown below. Thus, the main difference in the dense and porous films is that there is an order of magnitude more intense PL from the dense film and very weak quenching by oxygen. The penetration depth of the incident light at the 350 nm excitation wavelength is about 0.5 μm based on the absorption coefficient of ~20,000 cm^{-1} reported in ref 17. However, that data was for a mesoporous film of TiO_2 nanotubes; hence, the penetration depth in our dense thin film may be even smaller. The thickness of the dense film is about 0.8−1 μm and that of the ~50% porous nanocrystalline films is on the order of 10 μm. Thus, both films are thicker than the penetration depth of the incident light, and the intensity difference between them is not due to an increase in the amount of TiO_2 sampled in the dense film. We attribute the more efficient PL quenching by air in the case of the mesoporous film, which is approximately 50% porous, to the much larger surface area available for adsorption of O_2 and thus greater scavenging of conduction band electrons. As in the case of rutile[18] and other gas sensing oxides,[19−21] evidence suggests O_2 adsorbs on surface oxygen vacancies of anatase.

Becuse luminescent defects reside on the nanoparticle surface,[9,36] more intense PL from the dense film is surprising at first glance. However, the intensity of defect PL in TiO_2 also depends on carrier transport, which competes with radiative recombination, as well as the defect density. We hypothesize that more intense PL from the dense nanoparticle film results from grain boundaries, which impede interparticle electron transport. Carrier transport is related to the width of the neck between nanoparticles.[22] In the conceptual depiction of a TiO_2 gas sensor film,[23] particle interconnectivity is controlled to prevent transport of charges within the film, thus maximizing the charges available for the sensing mechanism. The different intensities of the dense and mesoporous films seen here might reflect differences in both carrier transport and defect density. This conclusion seems reasonable in light of studies that suggest the presence of grain boundary barriers associated with interface trap states[24,25] and that they have greater importance in microcrystalline as compared to nanocrystalline TiO_2 films.[26] The weaker quenching effect of ambient O_2 in the case of the dense TiO_2 films is attributed to the lower accessibility of oxygen vacancy binding sites at these buried interfaces. However, as shown in Figure S4 of the Supporting Information, O_2 has an increasingly greater quenching effect on the PL of samples calcined at 700, 800, and 900 °C than for the 600 °C sample, though never as large as the effect on the PL of a mesoporous film. On the basis of the Raman and X-ray data for the latter samples, we hypothesize that the amorphous TiO_2 content of the 600 °C sample, presumably on the surface, is unfavorable to binding O_2. At the same time, there is possibly an increase in the number of oxygen vacancies in the films annealed at higher temperatures.

Figure 2 shows the PL of undoped TiO_2 films that were subjected to calcination at 600, 700, 800, and 900 °C. In all cases, anatase is the majority phase as shown by Raman spectroscopy and XRD, with a small amount of rutile evident in the XRD of the 900 °C film. As shown in Figure S2 of the Supporting Information, the normalized intensity of the 143 cm^{-1} Raman peak shows little variation in width or frequency for the four samples. This peak is known to broaden and shift when significant numbers of oxygen vacancies are present.[27] However, the general increase in intensity of anatase Raman lines with higher calcination temperature is in agreement with an increase in crystallinity as reported in ref 15 on the basis of XRD and SEM images shown in the Supporting Information.

The samples calcined at 600 and 700 °C show only the visible PL of anatase, while the 800 and 900 °C samples reveal the near-IR PL of minor amounts of rutile. The quantum yield of rutile PL is orders of magnitude larger than that of anatase, making the PL spectrum much more sensitive for detecting small amounts of rutile. In addition, the conduction band edge of rutile is about 0.2 eV lower than that of anatase,[28] enabling interphasial transport of conduction band electrons from anatase to rutile. Between 600 and 700 °C there is a slight increase in anatase PL with no change in shape. This could be the result of enhanced crystallinity. We have shown that the photoluminescent hole and electron traps of anatase are sequestered on different exposed crystal planes of anatase.[10] (It is worth noting that the typical anatase PL shown in Figures 1 and 2 are not present in amorphous TiO_2 nanoparticles where more blue emission is observed.[29]) The slight increase in intensity of PL in the 700 °C sample compared to the 600 °C film could be correlated to enhanced crystallinity.[30] On increasing the calcination temperature from 700 to 800 °C, there is a further overall increase in the anatase PL accompanied by a blue-shift in

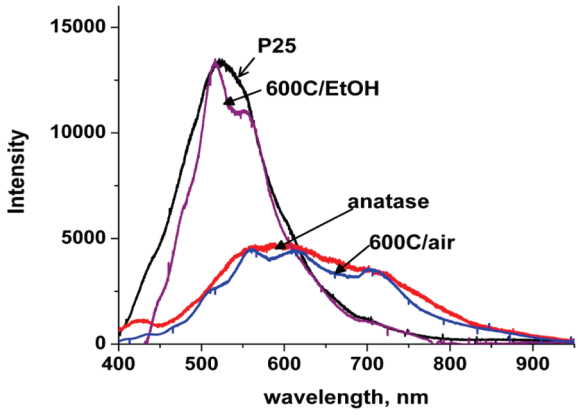

Figure 3. PL spectrum of a mesoporous anatase film normalized to the same maximum intensity as the PL of a dense 12-layer TiO_2 film calcined at 600 °C. The PL from the dense film in contact with ethanol (EtOH) is also shown compared to the spectrum of a mesoporous film of P25 measured in argon.

the peak. This blue-shift is associated with increased formation of oxygen vacancies[11] and correlates well with the decrease in baseline resistivity in this temperature range.[15] In addition, the near-IR PL of rutile emerges for the 800 °C sample. After calcination at 900 °C, there is an overall decrease in both the anatase and rutile components of the PL, despite the increase in rutile content. The peak at about 540 nm in the anatase PL for this sample is significantly less intense. This suggests quenching of the red-emitting electron traps as seen previously in mesoporous anatase films heated at 900 °C and also containing small amounts of rutile.[10] The rutile PL does not arise from defects but rather from holes trapped on 3-fold coordinated oxygen atoms of the exposed (110) and (100) surfaces.[13] Hence, the decrease in rutile PL from 800 to 900 °C could be the result of an increase in size of the rutile particles and thus a decrease in the surface-to-volume ratio. As reported previously, FE-SEM images and XRD reveal increase in grain size from 800 to 900 °C. This explains the overall decrease in the intensity of PL from surface defects. At the same time, less intimate connection of anatase and rutile phases in the 900 °C sample would decrease the ability of the rutile phase to act as a sink for conduction band electrons from anatase, also contributing to weaker rutile PL.

As shown in Figure S4 of the Supporting Information, the PL of the 12-layer dense films becomes more sensitive to oxygen for films subjected to higher calcination temperature. The PL of the 700 °C sample is slightly reduced in air compared to argon. This effect is small compared to the approximately 3-fold reduction in PL on exposing the 800 °C film to air. Exposure of the 900 °C film to air instead of argon resulted in almost complete quenching of the anatase emission with only a slight reduction in the rutile PL. These observations may indicate an increase in oxygen vacancy content in the 800 °C sample over that of the films calcined at lower temperature, which results in both more intense PL as well as greater sensitivity to O_2 as an electron scavenger. Increased oxygen vacancy content is also suggested by the decreased resistance of the films with increasing calcination temperature between 700 and 900 °C. Note that the near-IR PL from pure rutile nanoparticles is not very sensitive to oxygen.[10] Greater quenching of the rutile component of the PL by air in the case of the 800 °C versus the 900 °C sample is also evidence that the particles of the two phases are in better electrical contact in the former film than in the latter, accounting for the increased rutile emission in the 800 °C film.

Figure 3 shows the effect of the efficient hole scavenger ethanol (EtOH) on the PL from the 12-layer 600 °C film. In the presence of air, the PL from the dense film shows an envelope that matches the scaled PL spectrum from a mesoporous anatase film. Exposure of the dense films to EtOH shuts off the red PL from the recombination of trapped electrons with valence band holes, leaving a spectrum which resembles that of P25, which is in agreement with our previous results.[10] Thus, despite the smaller exposed surface area of the compact film compared to the mesoporous film, EtOH can still efficiently scavenge valence band holes. This is in contrast to effect of oxygen as an electron scavenger, for which scavenging depends on the accessibility of defect-related adsorption sites.

The PL of the dense film in Figure 3 shows definite structure that is not seen in thicker mesoporous films. These peaks were found to be more pronounced when the excitation beam was more tightly focused at the sample. Assuming that this structure results from interference, the thickness d of the film was calculated from $2n(\lambda)/\lambda = i/d$, where i is the peak number, and $n(\lambda)$ is the refractive index at wavelength λ. Taking $n(\lambda)$ as the average of the values at 320 and 400 nm for anatase,[31] the film thickness was calculated to be 1000 nm, in good agreement with the value taken from SEM images, i.e., between 800 and 1200 nm as reported in ref 34. This confirms that the structure in the spectra of Figures 2 and 3 is the result of interference.

The same defects that give rise to visible PL could also lead to band tails in the absorption spectrum.[16] An alternative explanation is that the band tails are associated with amorphous TiO_2, which decreases with increasing calcination temperature.[32] The absorption spectra of 2-layer films, which are thin enough for measurement in transmission, were obtained as a function of calcination temperature. Figure 4 shows the absorbance and PL spectra of 2-layer films that were subjected to calcination at 600, 700, 800, and 900 °C. The absorbance spectra in all films show a maximum at around 250 nm (4.9 eV) and a shoulder at 300 nm (4.1 eV). Some variations in the band tail region were present and showed the 700 °C film as having the largest maximum absorbance and the steepest absorption edge.

As shown in Figure 4, the PL spectra of the 2-layer films exhibit some important differences compared to the spectra of the thicker films shown in Figure 2. Interference fringes are absent as expected for the thinner film. Though the intensity trends with calcination temperature are similar to those seen in the thicker film, there is no hint of rutile emission, even for films calcined at 900 °C. In all cases, the visible emission from anatase shows a peak at about 550 nm, which is blue-shifted compared to the anatase PL from the thicker film. The most intense PL was observed in the film with the steepest band edge, calcined at 700 °C. However, there are no clear trends for the remaining films, and the variations in PL are much larger than the variations in the normalized absorption spectra. This lack of correlation may be tied to the importance of carrier transport in determining the intensity of the PL or may be a result of both amorphous material and oxygen vacancies contributing to the band tails.

The absence of a rutile peak, even for the 900 °C sample, may be related to the size-dependent stability of anatase and rutile nanoparticles.[33] The rutile phase is favored for crystallite dimensions above 50 nm; therefore, the 140−160 nm thickness of the 2-layer film is not as favorable to rutile nanoparticle formation as the thicker (~1000 nm) films. Another striking difference

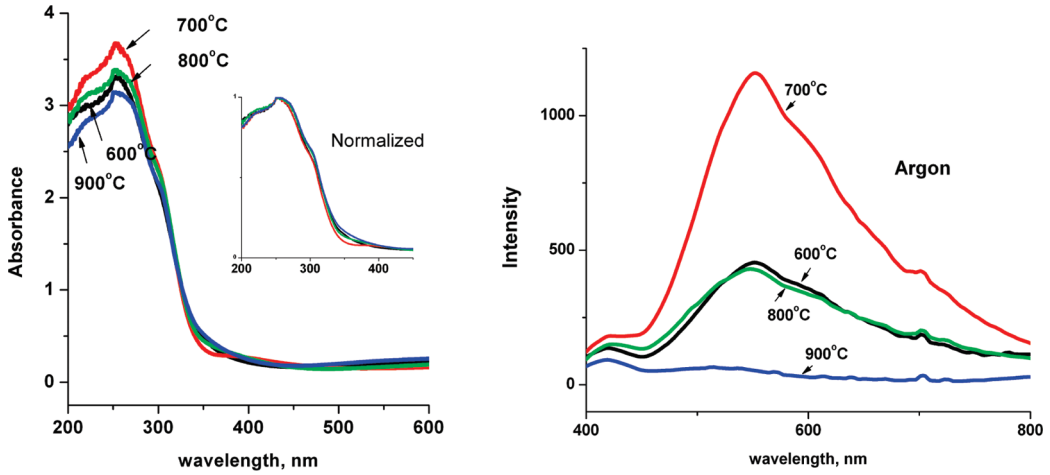

Figure 4. Absorbance (left) and photoluminescence (right) of 2-layer dense films of nanocrystalline anatase, as a function of calcination temperature. The inset shows the absorbance spectra normalized to the same maximum. The PL spectra were recorded in argon.

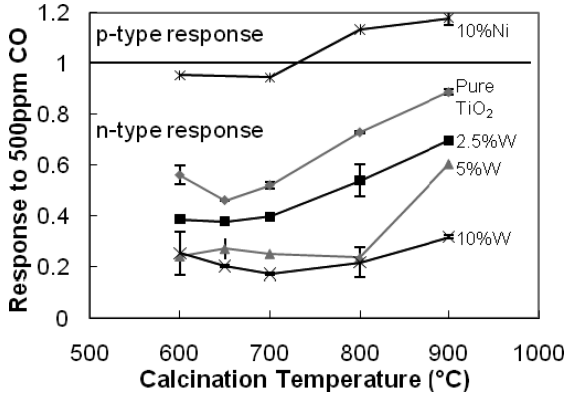

Figure 5. Performance of W- and Ni-doped films as CO sensors compared to that of pure TiO_2.

compared to the thick films is the greater sensitivity to oxygen in the case of the 2-layer films. The PL data shown in Figure 4 were recorded in argon and can be compared to the same data recorded in air where the intensity is reduced by roughly a factor of 2 (Figure S5 of the Supporting Information). This is attributed to the larger ratio of exposed surface area to illuminated volume. Because the PL spectra of the thin and thick films were recorded with the same incident power density, the appearance of a peak in the green for thin layer films corresponds to a higher photogeneration rate of electron−hole pairs, and thus, PL is dominated by the radiative recombination of conduction band electrons with trapped holes.

2. Doped Thin Films. The thin films were doped with nickel and tungsten resulting in either p-type or n-type electrical behavior, respectively. The following defect reactions occur upon doping

$$TiO_2 \xrightarrow{W} W_{Ti^{4+}}^{6+\bullet\bullet} + 2O_O^X + 2e' \quad (2)$$

$$TiO_2 \xrightarrow{Ni} Ni_{Ti^{4+}}^{2+} + 2O_O^X + 2h^{\bullet} \quad (3)$$

Calcining of films doped with aliovalent cations nickel and tungsten was done at different temperatures for each dopant because of the different phase stability of the anatase−rutile transformation in doped TiO_2 and to avoid the formation of unwanted phases such as tungsten oxide with increasing heat treatment temperature.[34] As shown by the XRD (Figure S6 of the Supporting Information) and Raman spectra (Figure S3 of the Supporting Information), the W-doped film calcined at 700 °C is in the anatase phase, while the Ni-doped film at 900 °C shows conversion to rutile, even though the undoped sample at this temperature remained predominantly in the anatase phase. This is evidence that nickel as a substitutional impurity enhances the formation of rutile in accord with similar observations in the literature.[38]

Figure 5 shows the performance of the doped and undoped samples as sensors for CO. We found that incorporating tungsten strongly enhanced the n-type conduction, while nickel created some p-type conduction. The dopants had the same effect on gas response: increased n-type response for W-doped and p-type response for Ni-doped sensors. The most notable influence of the dopants (especially tungsten) was that their effect on the sensing performance seemed to be somewhat independent of the grain size or amount of rutile formation [i.e., the 10% W sample calcined at 600 (100% anatase)] had the same good n-type response as the 10% W sample calcined at 900 (nearly all rutile). These results indicated that the extrinsic defects from the addition of tungsten dominated the sensing response irrespective of the microstructure or crystalline phase. The W-doped samples outperformed pure TiO_2, and the best performance was found for the 10% W sensor.

The PL spectra of the doped films are shown in Figure 6. In the case of tungsten, dopant concentrations from 2.5% to 10% result in a strong green PL, consistent with the greater availability of mobile electrons in this n-doped sample. The intensity of PL decreases with increasing W content, suggesting that the dopant itself is acting as a donor rather than merely facilitating the formation of oxygen vacancies. The weak yellow coloration of the W-doped films raises the question as to whether the changes in PL of Figure 6 are the result of self-absorption of the emitted light. However, this can be ruled out because the presence of W extends the absorption band edge into the blue and cannot account for reduced intensity of the PL at more red wavelengths.

In the case of the Ni-doped sample, for which both XRD and Raman reveal complete conversion to rutile on calcination at

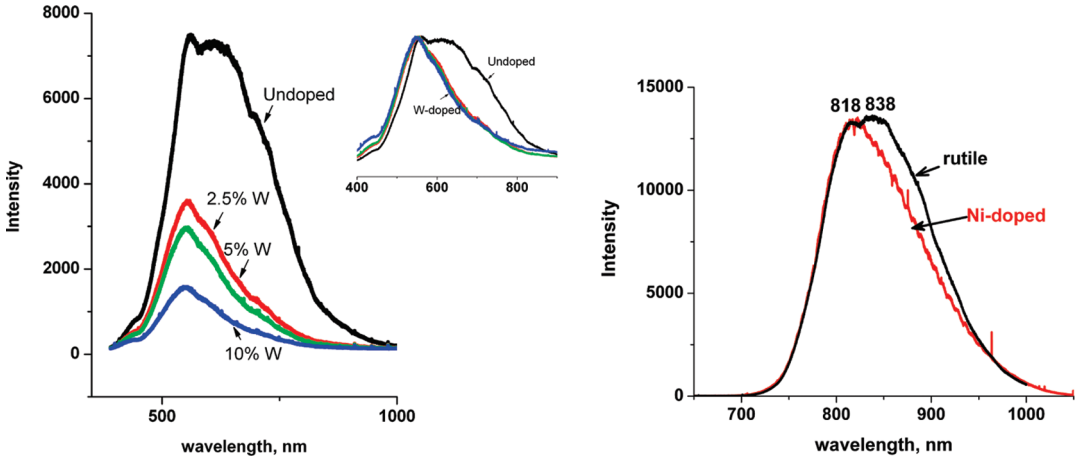

Figure 6. PL spectra of W-doped (left) and Ni-doped 12-layer films calcined at 700 and 900 °C, respectively, and recorded in argon. The inset at left shows the spectra of the W-doped films scaled to the same maximum. The PL of the Ni-doped film at right is compared to a scaled PL spectrum of a mesoporous film of rutile nanoparticles from ref 10.

900 °C, the near-IR PL shown in Figure 6 is characteristic of the rutile phase as expected. Interestingly, the Ni-doped film shows a peak at about 820 nm corresponding to the holes trapped on the (110) surface, while the 840 nm peak associated with the (100) surface is absent.[13] The absence of PL from the (100) surface may be the result of the nature of the growth of the rutile particles from the pre-existing anatase particles.

3. Relation to Gas Sensing. Gas sensor performance is gauged through the ratio of film resistance exposed to the target gas against the resistance when exposed to the background gas.[34] For films prepared by the same sol−gel method used in the present work, gas sensing was optimal when films had been calcined at 600−700 °C (Figure 5, ref 34). This was attributed to the competing effects of particle size and crystallinity, which both increase with calcination temperature. While enhanced crystallinity is favorable to the response, it comes at the expense of decreased surface area for gas adsorption. Evidence exists that for TiO_2 in both the rutile[18,39] and the anatase[32] phases, O_2 is adsorbed in the immediate neighborhood of a vacancy where it scavenges trapped electrons. These vacancies give rise to the defect PL and also provide binding sites that allow O_2 to quench the PL through electron scavenging. The ratio, therefore, of the photoluminescence in argon and to that in air might be expected to correlate to the sensitivity of the film's resistance to its environment. In undoped samples, the ratio most different from unity was seen in the film calcined at 800 °C, followed by 900 °C, then by 700 °C (Figure S4 of the Supporting Information). However, as shown in Figure 5, the response to CO was larger for the films calcined at 600−700 °C, for which there is only a small effect of air on the intensity of PL. The basis for this apparent discrepancy may lie in the competing effects of defect density and transport on the intensity of anatase PL and the extraordinary role of minor amounts of rutile. For the undoped sample calcined at 800 °C, the PL spectrum showed evidence of rutile even though the amount is too low to be detected by XRD or Raman. Thus, although the PL for this film in air reveals efficient electron scavenging by adsorbed oxygen, the transport is dominated by rutile sinks, and thus, the film resistance is not as oxygen-dependent as that of the films calcined at lower temperature and lacking the rutile phase. It is possible that while higher calcination temperature improved the crystallinity of the films (allowing for more oxygen vacancies to be close to the surface), the transport of the charges is also improved. One important thing to keep in mind is the difference in conditions between PL measurements and resistivity testing. Sensing tests were performed at higher temperatures, and the absorption and desorption reactions may occur at different rates at room temperature.

Oxygen vacancies are sites of O_2 adsorption and dissociation,[39] and the adatom formed reacts with the target gases (carbon monoxide for instance) causing the change in film resistance. From the defect reactions, doping with tungsten creates n-type carriers; creation of oxygen vacancies also results in similar charges. As mentioned earlier, the PL decreased upon addition of small amounts of tungsten supporting the possible consequence of tungsten-doping as pointed out by the defect reaction, which is the decrease in the driving force for oxygen vacancy formation. W-doping improves the gas response ratio, despite the apparent decrease in number of oxygen vacancies as judged by the decrease in PL intensity. As shown in Figure S9 of the Supporting Information, however, the W-doped samples annealed at 700 °C undergo significant quenching by air, on the order of 40 to 60%, compared to only about 25% quenching for the undoped sample annealed at the same temperature. In the case of the W-doped samples, we do not see evidence for rutile sinks, and the effect of air on the PL does appear to correlate with the improved gas response ratio in the W-doped sample. Thus, the W-doped samples display good response as sensors despite apparently fewer oxygen vacancies.

To understand this, it is important to note the source and location of the dissociation of O_2. Studies by Du et al.[39,18] on rutile surfaces show that the charges that transfer from the surface to the adsorbed O_2 are electrons from oxygen vacancies, and that these charges can migrate through the lattice making them delocalized over the vicinity of the vacancy. This means that not just a single oxygen vacancy contributes its charge to the dissociation but several. From ref 18 also, the O_2 dissociation was seen to be on the Ti rows, where the electrons are delocalized. Upon tungsten doping, the carrier charges (electrons) are still created upon substitution, and these could still travel to the surface. Although this study was done in rutile (110) surfaces, similar behavior is thought to be the reason for the improved gas sensing with tungsten doping. In undoped samples, the charges are associated with the creation of oxygen vacancies, which were

seen to be healed by some O-adatoms; thus, there are fewer O-adatoms available for the reaction with target gases. On the other hand, W-doping makes more n-type carriers or electrons available for dissociation of O_2, and more O-adatoms are created and available for the reaction with target gases. Nickel-doped samples showed the presence of a significant amount of rutile and have been observed to have p-type conductivity[1] at elevated temperatures and are seen to be responsible for the p-type sensor behavior.[34]

CONCLUSIONS

The photoluminescence of titanium dioxide is an indication of the number of intraband gap states and the efficiency of carrier transport. The much larger PL intensity from the dense nanocrystalline films used as sensors, as compared to previously studied porous nanocrystalline films, is attributed to the larger number of grain boundaries in the former, which impede the carrier transport that competes with radiative recombination of trapped and mobile charges. The PL from dense films is also much less quenched by oxygen than that of porous films because the O_2 binding sites at buried interfaces are less accessible.

Our previously reported data suggests that the green PL of anatase is attributable to oxygen vacancies.[11] The difference in the PL intensity for the same sample in argon and in air shows the relative number of sites that are available to bind electron-scavenging O_2. Though this difference is larger in the samples calcined at higher temperatures, 800 and 900 °C, the presence of rutile in these samples results in interphasial electron transport and decreases the sensitivity of the sensor to the target gas. Rutile is stable at larger dimensions, and by limiting the sample thickness to approximately 150 nm, its formation can be suppressed. Tungsten doping results in an overall decrease in the PL with increasing amount of dopant, suggesting a decrease in the number of oxygen vacancies while keeping the carriers required for O_2 dissociation. Nickel doping lowers the transformation temperature of anatase to rutile, resulting in a large percentage of rutile in the doped sample leading to its p-type sensor behavior.

The present results demonstrate that photoluminescence is a more sensitive measure of minor amounts of rutile in the majority anatase phase than is Raman and XRD. Though higher calcination temperatures promote the conversion of amorphous material to crystalline anatase, the concurrent emergence of rutile, as revealed by the PL spectra, dominates the carrier transport owing to its ability to act as a sink for conduction band electrons, resulting in reduced gas sensor response. The present results also confirm our hypothesis that luminescent defects reside on specific crystal planes, resulting in increased intensity of PL and increased number of oxygen-binding defects for films with improved crystallinity, as confirmed by XRD and Raman.

ASSOCIATED CONTENT

Supporting Information. XRD (Figure S1), Raman (Figure S2), and SEM images (Figure S3) of undoped films as a function of calcination temperature; photoluminescence of undoped 12-layer films (Figure S4) and 2-layer films (Figure S5) in argon and air as a function of calcination temperature; XRD (Figure S6), Raman and PL (Figure S7), and SEM images (Figure S8) of W- and Ni-doped films; and PL of W-doped films in air and argon (Figure S9). This information is available free of charge via the Internet at http://pubs.acs.org/.

AUTHOR INFORMATION

Corresponding Author
*E-mail: jmchale@wsu.edu.

ACKNOWLEDGMENT

Susmita Bose and Amit Bandyopadhyay thank the Office of Naval Research for Grant N00014-1-05-0583.

REFERENCES

(1) Nowotny, M.; Sheppard, L.; Bak, T.; Nowotny, J. *J. Phys. Chem. C* **2008**, *112*, 5275–5300.
(2) Kofstad, P. *Nonstoichiometry, Diffusion, and Electrical Conductivity in Binary Metal Oxides*: Wiley: New York, 1972.
(3) Mandelis, A.; Christofides, C. *Physics, Chemistry and Technology of Solid State Gas Sensor Devices*: Wiley: New York, 1993.
(4) Kuznetsov, V. N.; Serpone, N. *J. Phys. Chem. B* **2006**, *110*, 25203–25209.
(5) Huang, X. *Sens. Actuators, B* **2004**, *99*, 444–450.
(6) Dutta, P. K.; Ginwalla, A.; Hogg, B.; Patton, B. R.; Chwieroth, B.; Liang, Z.; Gouma, P.; Mills, M.; Akbar, S. *J. Phys. Chem. B* **1999**, *103*, 4412–4422.
(7) Berger, T.; Sterrer, M.; Diwald, O.; Knözinger, E.; Panayotov, D.; Thompson, T. L.; Yates, J. T. *J. Phys. Chem. B.* **2005**, *109*, 6061–6068.
(8) Yoshihara, T.; Tamaki, Y.; Furube, A.; Murai, M.; Hara, K.; Katoh, R. *Chem. Phys. Lett.* **2007**, *438*, 268–273.
(9) Knorr, F. J.; Zhang, D.; McHale, J. L. *Langmuir* **2007**, *23*, 8686–90.
(10) Knorr, F. J.; Mercado, C.; McHale, J. L. *J. Phys. Chem. C* **2008**, *112*, 12786–12794.
(11) McHale, J. L; Rich, C. C.; Knorr, F. J. MRS Spring 2010 Conference Proceedings, 1268-EE03−08.
(12) Jung, K. Y.; Park, S. B.; Anpo, M. *J. Photochem. Photobiol. A* **2005**, *170*, 247–252.
(13) Imanishi, A.; Okamura, T.; Ohashi., N.; Nakamura, R.; Nakato, T. *J. Am. Chem. Soc.* **2007**, *129*, 11569–11578.
(14) Kopidakis, N.; Benkstein, K. D.; van de Lagemaat, J.; Frank, A. J. *J. Phys. Chem. B* **2003**, *107*, 11307–11315.
(15) Seeley, Z. A.; Bandyopadhyay, A.; Bose, S. *Thin Solid Films* **2010**, *519*, 434–438.
(16) Zhang, D.; Downing, J. A.; Knorr, F. J.; McHale, J. L. *J. Phys. Chem. B* **2006**, *110*, 21890–21898.
(17) Mor, G. K.; Grimes, C. A. *Sol. Energy Mater. Sol. Cells* **2006**, *90*, 2011–2075.
(18) Du, Y.; Deskins, N. A.; Zhang, Z.; Dohnalek, Z.; Dupuis, M.; Lyubinetsky, I. *Phys. Chem. Chem. Phys.* **2010**, *12*, 6337–6344.
(19) Brinzari, V.; Korotcenkov, G.; Golovanov, V. *Thin Solid Films* **2001**, *391*, 167–175.
(20) Vlachos, D. S.; Papadopoulos, C. A.; Avaritsiotis, J. N. *J. Appl. Phys.* **1996**, *80*, 6050–6054.
(21) Gaggiotti, G.; Galdikas, A.; Kačiulis, S.; Mattogno, G.; Setkus, A. *J. Appl. Phys.* **1994**, *76*, 4467–4471.
(22) Cass, M. J.; Qiu, F. L.; Walker, A. B.; Fisher, A. C.; Peter, L. M. *J. Phys. Chem. B* **2003**, *107*, 113–119.
(23) Akbar, S.; Younkman, L. *J. Electrochem. Soc.* **1997**, *144*, 1750–1753.
(24) Rothschild, A.; Komem, Y.; Levakov, A.; Ashkenasy, N.; Shapira, Y. *Appl. Phys. Lett.* **2003**, *82*, 574.
(25) Baumann, S. O.; Elser, M. J.; Auer, M.; Bernadi, J.; Hüsing, N.; Diwald, O. *Langmuir* **2011**, *27*, 1946–1953.
(26) Demetry, C.; Shi, X. *Solid State Ionics* **1999**, *118*, 271–279.
(27) Parker, J. C.; Siegel, R. W. *Appl. Phys. Lett.* **1990**, *57*, 943–945.
(28) Barbe, C. J.; Arendse, F.; Camte, P.; Jirousek, M.; Lenzmann, F.; Shklover, V.; Grätzel, M. *J. Am. Ceram. Soc.* **1997**, *80*, 3157–71.
(29) Ghosh, H. N.; Adhikari, S. *Langmuir* **2001**, *17*, 4129–4130.

(30) Seeley, Z. M.; Bandyopadhyay, A.; Bose, S. *Mater. Sci. Eng., B* **2009**, *164*, 38–43.
(31) Tanemura, S.; Miao, L.; Jin, P.; Kaneko, K.; Terai, A.; Nabatova-Gabain, N. *Appl. Surf. Sci.* **2003**, *212−213*, 654–660.
(32) Bilmes, S. A.; Mandelbaum, P.; Alvarez, F.; Victoria, N. M. *J. Phys. Chem. B* **2000**, *104*, 9851–9858.
(33) Chen, X.; Mao, S. S. *Chem. Rev.* **2007**, *107*, 2891–2959.
(34) Seeley, Z. M. Ph.D. Thesis, Washington State University, December 2009.
(35) Savage, N.; Chwieroth, B.; Ginwalla, A.; Patton, B. R.; Akbar, S. A.; Dutta, P. K. *Sens. Actuators, B* **2001**, *79*, 17–27.
(36) Naisbitt, S. C.; Pratt, K. F. E.; Willimas, D. E.; Parkin, I. P. *Sens. Actuators, B* **2006**, *114*, 969–977.
(37) Kopidakis, N.; Neale, N. R.; Zhu, K.; van de Lagemaat, J.; Frank, A. J. *Appl. Phys. Lett.* **2005**, *87*, 202106.
(38) Gole, J.; Prokes, S.; Glembocki, O. *J. Phys. Chem. C* **2008**, *112*, 1782–1788.
(39) Du, Y.; Dohnalek, Z.; Lyubinetsky, I. *J. Phys. Chem. C* **2008**, *112*, 2649–2653.